Desalination and Water Treatment
www.deswater.com
doi: 10.5004/dwt.2023.29838

306 (2023) 189–198
September

Facile preparation of apatite nanostructures and their potential application in water treatment

Junfeng Zhao[a,b], Zichen Wang[a], Zhi Tang[a], Meiqi Hui[a], Shilong Yin[a,b,*]

[a]*School of Materials Engineering, Changshu Institute of Technology, Changshu, Jiangsu 215500, China, email: yinshilong2008@163.com*
[b]*Suzhou Key Laboratory of Functional Ceramic Materials, Changshu Institute of Technology, Changshu, Jiangsu 215500, China*

Received 9 February 2023; Accepted 1 August 2023

ABSTRACT

A novel precipitation route has been developed for synthesis of hydroxyapatite (HAp) and chlorapatite (ClAp) powders. The powders were characterized by X-ray diffraction, Fourier-transform infrared spectroscopy, scanning electron microscopy, transmission electron microscopy, and nitrogen adsorption–desorption techniques. The results showed that the as-prepared products were the nanostructures consisting of HAp and ClAp nanoparticles with a large surface area of 104.4 and 90.9 $m^2 \cdot g^{-1}$, respectively. The as-prepared products were respectively used as an absorbent for the removal of Congo red (CR) from simulated wastewater. The maximum adsorption capacity for CR onto HAp and ClAp nanoparticles was determined using the Langmuir equation and found to reach up to 512.78 and 542.27 $mg \cdot g^{-1}$, respectively. The apatite such as HAp and ClAp is potential absorbents for use in dye pollution removal if synthesized on a large scale, a low price and a fast solid–liquid separation in the near future.

Keywords: Hydroxyapatite (HAp); Chlorapatite (ClAp); Nanostructures; Dye removal; Congo red

1. Introduction

Global water demand is projected to increase by at least 55% by 2050 mainly due to high GDP growth rate that will increase water demand for manufacturing, power generation and domestic sector use by 400%, 140% and 130%, respectively [1–3]. This current demand trend will push 40% of the world population below water scarcity level by 2050 [1]. Whereas, with the aggravation of the global environmental crisis, especially the rapid progress of industry and development of society, water pollution is becoming increasingly serious [4]. Dyes and their effluent are one of the main sources of water pollution, and cause many detrimental effects on environment and severe health problems in human beings [5]. Therefore, the efficient removal of dye pollutants from water has become an urgent problem at present [6]. So far, many effective methods have been adopted, including coagulation [7], chemical oxidation [8], adsorption [9], and electrochemical processes [10] for the removal of organic dyes. Among them, the adsorption onto the surface of the solid materials is a common way for the water treatment because of its high performance, relatively low capital and operational costs [11]. Especially, the development of nano-absorbents has opened up new ideas for the wastewater treatment because of their large surface area, high density of available surface adsorption sites, surface defects, fast diffusivities and well-defined morphology. To date, various absorbents such porous nanostructures [12,13], carbon nanotube [14], oxide particles [15,16], and magnetic composites [17] have been developed for the treatment of dye pollutions. However, low adsorption capacity, high cost and the difficulty of separation restrict their industrial applications. It is therefore a very meaningful issue to develop the low-cost absorbents with high adsorption capacity.

The calcium phosphate apatite including hydroxyapatite (HAp, $Ca_{10}(PO_4)_6(OH)_2$) and chlorapatite (ClAp,

* Corresponding author.

$Ca_{10}(PO_4)_6Cl_2$) has been used for various biomedical applications in the manufacture of bone cements, toothpaste additive, monolithic implants and drug carrier due to its biocompatibility, bioactivity, osteoconductivity and nontoxicity [18]. Recent reports also showed that HAp hold great promise in removal of heavy metal ions and organic compounds from wastewater due to its specific structure conferring ionic exchange property and adsorption affinity towards many pollutants [19]. Various synthesis methods have been reported for the preparation of HAp nanostructures, such as hydrothermal [20], sol–gel [21], sonochemical [22], precipitation [23], microemulsion [24], microwave [25], mechanochemical [26] and self-propagating combustion method [27]. Among these methods, precipitation method has significant advantages such as low-cost, simple equipment's, easy preparation, short reaction time and better repeatability to obtain desired products. However, the adsorption of Congo red (CR) using HAp and ClAp as an absorbent has not been reported up to now.

In the present paper, pure HAp and ClAp nanostructure powders synthesized via a novel precipitation route were evaluated for their potential to the removal Congo red (CR) from simulated wastewater. The effect of adsorption time and initial concentration on the adsorption capacity, and the adsorption isotherms and kinetics were studied to clarify the adsorption process.

2. Experimental set-up

2.1. Materials

All of the chemical reagents, such as calcium nitrate tetrahydrate ($Ca(NO_3)_2{\cdot}4H_2O$), calcium chloride ($CaCl_2$), diammonium phosphate ($(NH_4)_2HPO_4$), ethanol amine (ETA), and Congo red (CR) are of analytical grade and used without further purification.

2.2. Synthesis of HAp and ClAp

The flowchart for preparing HAp and ClAp by the precipitation method is shown in Fig. 1. Two series of powders were synthesized with two different calcium sources (for HAp: using $Ca(NO_3)_2{\cdot}4H_2O$ and for ClAp: using $CaCl_2$). At first, 0.01 mol of $Ca(NO_3)_2{\cdot}4H_2O$ or $CaCl_2$ was added into 30 mL of ETA, then putted into an ordinary ultrasonic cleaner with a 80 kHz operating frequency for some minutes till completely dissolving into ETA to form a clear solution. 0.006mol of $(NH_4)_2HPO_4$ was dissolved in 50 mL of deionized water, and then the $(NH_4)_2HPO_4$ aqueous solution was added drop wise into the $Ca(NO_3)_2{\cdot}4H_2O$ or $CaCl_2$ aqueous solution under vigorous stirring for 2 h. The precipitation was washed by deionized water until it became neutral and then was dried at 80°C for 24 h. Finally, the dried precipitation was calcined at 600°C for 3 h to obtain samples.

2.3. Characterization

The crystalline structure was described by X-ray diffraction (XRD, Dmax-2200PC) with CuKα radiation (40 kV, 40 mA) and step size of 0.02° and a present time of 4 s. The spectra were compared to standard spectra from the Joint Committee on Powder Diffraction Standards (JCPDS) database. The Rietveld analysis was performed on the diffraction patterns using the program MAUD. The field-emission scanning electron microscopy morphology (FE-SEM) and the energy-dispersive X-ray spectrum (EDX) were conducted on Zeiss Sigma field-emission scanning electron microscope. Transmission electron microscopy (TEM) analysis was performed by means of JEM-2000. The surface areas of the powders were measured by Brunauer–Emmett–Teller method (ASAP 2020). Fourier-transform infrared spectroscopy (FTIR) (Nicolet 380) was carried out at room temperature in the range of 400–4,000 cm^{-1} using samples in the form of pellets formed with spectroscopic grade KBr. The precursors were also examined by thermogravimetric and differential thermal analyses (TG/DSC, Netzshch STA449F3C) at a heating rate of 20°C/min, from ambient to 800°C.

2.4. Adsorption experiments

Congo red (CR) was chose as the model to evaluate the dye adsorption activity of HAp and ClAp. Typical experiment for the adsorption of CR was performed as the following way. 0.1 g of HAp or ClAp was mixed with 100 mL of aqueous solution of CR with various concentrations (100, 300, 400, 500, 600 and 800 $mg{\cdot}L^{-1}$). With different time intervals, 5 mL of the solution was taken out for centrifuged. The concentration in the remaining solutions was analyzed by UV-Vis spectroscopy at λ_{max} = 498 nm.

3. Results and discussion

3.1. Characterization of the precursor

Fig. 2a shows the XRD patterns of the precursors without thermal treatment. The ClAp precursor contains a small

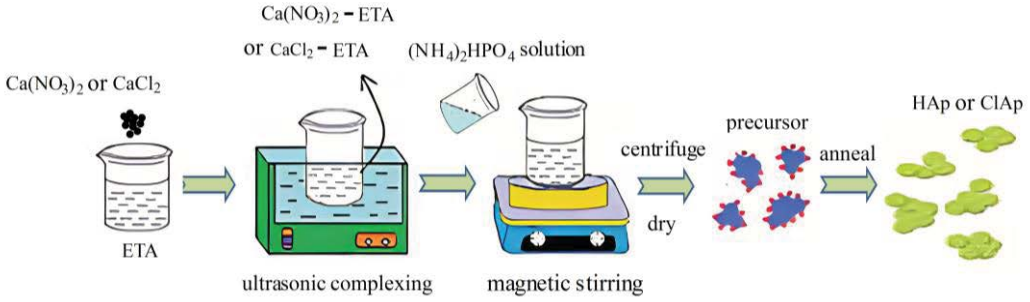

Fig. 1. Flowchart for preparing powder by the precipitation method.

amount of poorly crystalline apatite. For the HAp precursor, a gradual improvement in crystallinity (in terms of peak sharpness and intensity) of the apatite phase is observed.

FTIR spectroscopy is a useful tool to identify the functional group of any organic molecule. The FTIR spectrum of the precursors is shown in Fig. 2b. The peaks located at 3,140 and 3,430 cm^{-1} correspond to the N–H asymmetry stretching vibration. The peaks located at 1,400 and 1,630 cm^{-1} result from the C–N stretching and NH_2 scissoring [28]. This observation indicates the existence of ETA molecules in the precursors. The peaks located at 574, 604 and 1,030 cm^{-1} are the fundamental vibration modes of PO_4^{3-} group. The peak located at 830 cm^{-1} for HAp precursor corresponds to the vibration of NO_3^{2-}.

Fig. 2c and d show the TG/DSC trace of the precursors heated in flowing air. As shown in Fig. 2c, the DSC trace of the HAp precursor exhibits a strong endothermic peak and two exothermic peaks in the temperature ranging from 30°C to 800°C. The endothermic peak at about 78°C is attributable to the evaporation of the absorbed water. The two exothermic peaks at 272°C and 393°C are attributed to decomposition of nitrate and organic substance, respectively. The TG curve for HAp precursor is divided into three stages. The first stage, which is from room temperature to 250°C with a weight loss of 12%, is attributed to the evaporation of the absorbed water. The second stage, which is from 250°C to 360°C with a weight loss of about 11%, results from the decomposition of nitrate and the carbonization of organic substance. The third stage, which is from 360°C to 500°C with a weight loss of about 4%, is caused by the decomposition of residual organic materials. No obvious weight loss can be observed from 500°C to 800°C. Fig. 2d shows the TG/DSC curves for ClAp precursor. It can be seen that there is an endothermic peak and two exothermic peaks from 30°C to 800°C. The first endothermic peak appearing at 93°C corresponds to the evaporation of the absorbed water. The exothermic peak at 230°C results from the combustion and carbonization of organic substance. The last broad exothermic peak at around 380°C is attributed to the remove of residuals of organic compounds. The TG trace showed a total weight loss of 38% during heated treatment, including the evaporation of the absorbed water and the decomposition of the organic compounds.

The possible formation mechanism of precursor is shown in Fig. 3. At first, the in situ formation of (Ca-ETA) M_2(M = NO_3 or Cl) (complexes 1) may occur through the reaction between CaM_2 and ETA under ultrasonication. Then, the $(NH_4)_2HPO_4$ was added into complex 1 under magnetic stirring to form (Ca-ETA)M(PO_4) (complex 2).

3.2. Characterization of the powders

X-ray diffraction patterns of powders are shown in Fig. 4. Two major characteristic diffraction peaks can be

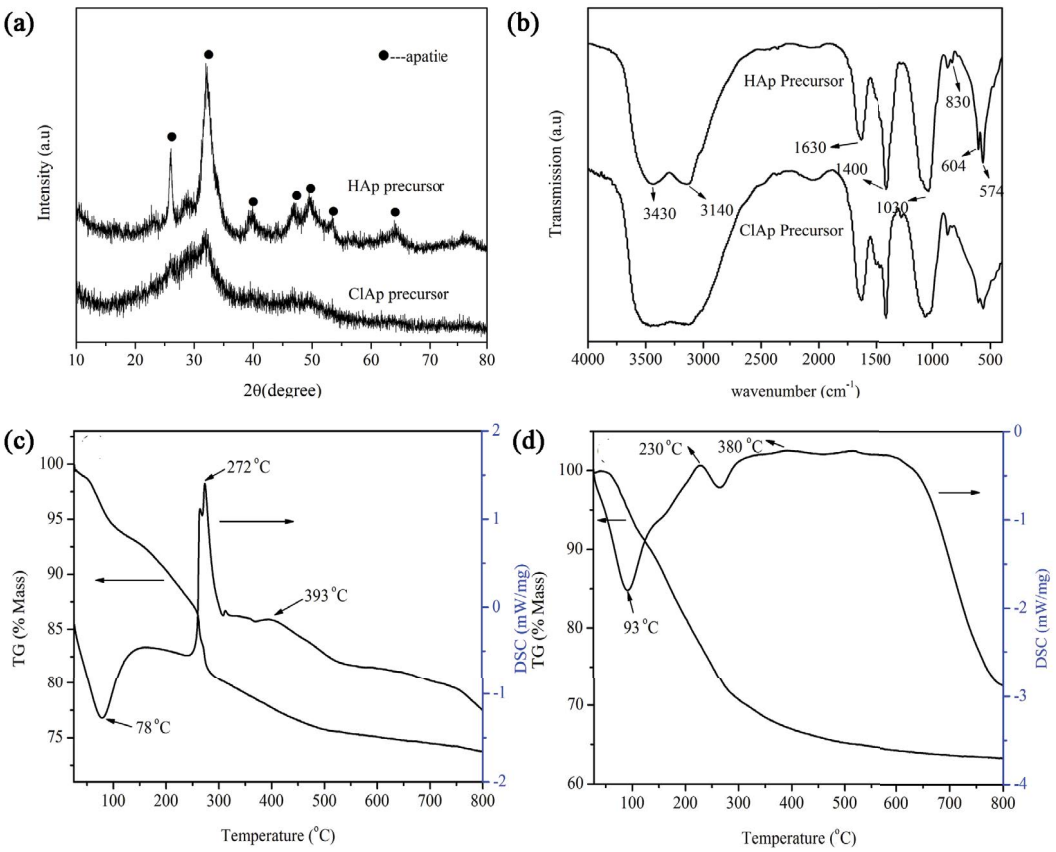

Fig. 2. (a) X-ray diffraction patterns of the precursors before annealing, (b) FTIR spectra of the precursors before annealing, and TG/DSC traces of the precursors heated in flowing air (c) HAp precursor, and (d) ClAp precursor.

obtained for the sample synthesized at 600°C: one closed at 2θ of ~26° and the other broad at ~32°, which can be indexed as a poorly crystalline calcium deficient apatite structure (Powder Diffraction File 9-432 JCPDS 2000). The XRD results show that $CaCl_2$ as calcium source is different to that of $Ca(NO_3)_2{\cdot}4H_2O$. According to the detailed analysis of patterns, the crystalline ClAp structure (Powder Diffraction File 27-0074 JCPDS 2000) is present in the sample. The mineralogical composition was determined by Rietveld refinement from XRD date. The lattice parameters extracted from Rietveld refinements are listed in Table 1. Fig. 4b and c show the resulting plot of a Rietveld refinement of the two samples. The two series show the presence of pure HAp and ClAp, respectively.

FTIR spectra of the powders as shown in Fig. 5 also confirm the formation of apatite phase in all the samples

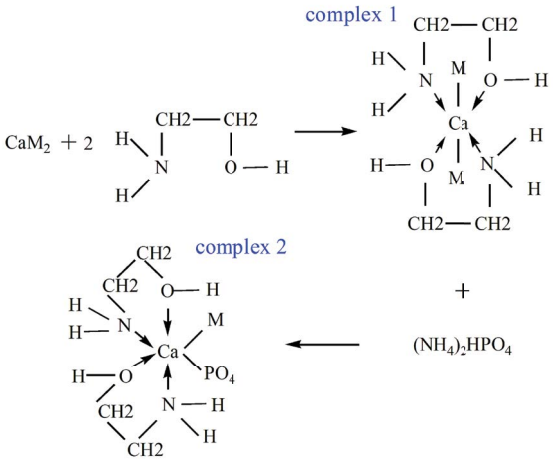

Series	M	Complex 1	Complex 2
1	NO_3^-	$Ca(TEA)_2(NO_3)_2$	$Ca(TEA)_2(NO_3)(PO_4)$
2	Cl^-	$Ca(TEA)_2Cl_2$	$Ca(TEA)_2Cl(PO_4)$

Fig. 3. Possible formation mechanism of precursor.

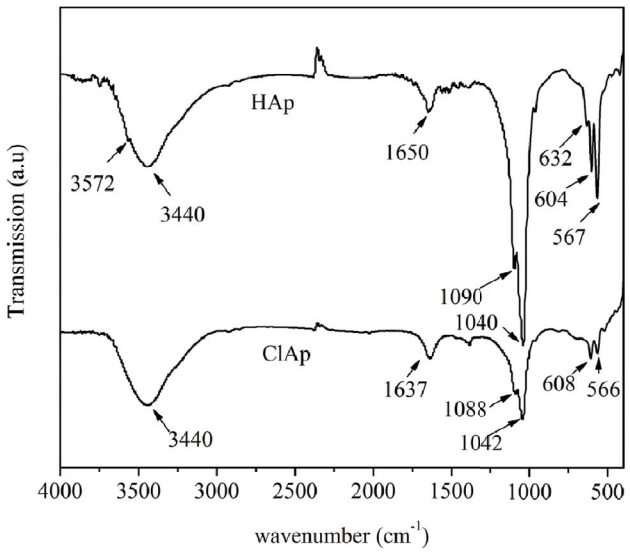

Fig. 5. FTIR spectra for HAp and ClAp samples.

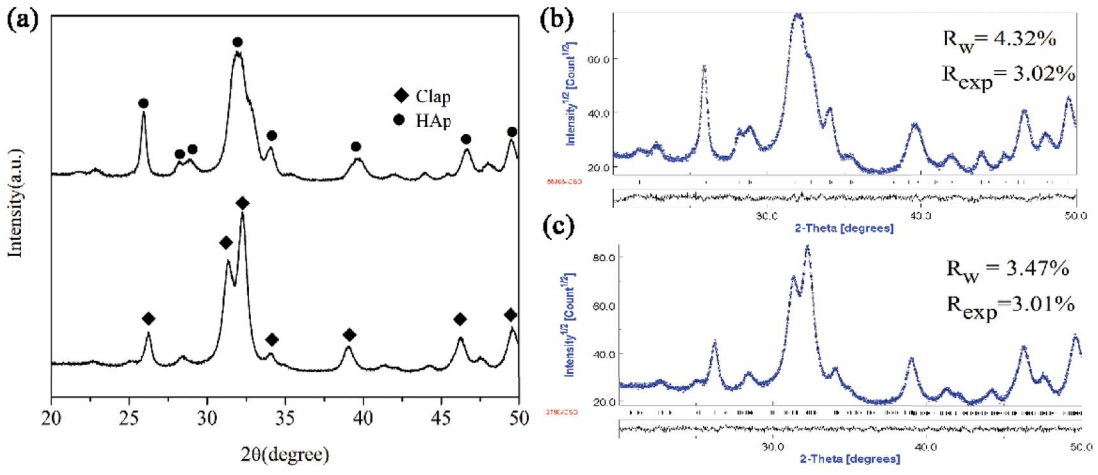

Fig. 4. (a) X-ray diffraction patterns of the synthesized powders, (b) Rietveld refinement for the HAp powders, and (c) ClAp.

Table 1
Lattice parameters extracted from Rietveld refinements

Phase		Lattice parameters			Structural model
Name	Formula	α (Å)	*b* (Å)	*c* (Å)	ICSD code
HAp (hydroxyapatite)	$Ca_5(PO_4)_3(OH)$	9.4528	9.4528	6.8714	56,306
ClAp (chlorapatite)	$Ca_5(PO_4)_3Cl$	9.6395	19.2166	6.7981	2,789

with the fundamental vibrational modes of PO_4^{3-} group near 567, 604, 1,040 and 1,090 cm^{-1}. The bands at about 567 and 604 cm^{-1} are attributed to the υ_4 vibration of the O–P–O mode. The bands at about 1,040 and 1,090 cm^{-1} correspond to the υ_4 vibration of the PO_4^{3-}. The bands at 3572 and 632 cm^{-1} are attributable to the vibrations of OH^- ions, which also confirms the formation of HA structure. Notably, the FTIR patterns reveal that the peaks related to the OH^- groups are not significant for the ClAp sample, which might result from the complete replacement of OH^- by the Cl^-.

Fig. 6 shows the scanning electron microscopy (SEM) micrographs of samples annealed at 600°C. It can be observed from the figure particle morphology varies significantly between the two samples. HAp sample in Fig. 6a shows the formation of rod-like nanoparticles, while ClAp sample in Fig. 6b exhibits irregular shapes with agglomeration. The energy-dispersive X-ray spectra of the two samples clearly revels the contents of Ca, P, and O in HAp sample, along with that of Cl in the ClAp sample. TEM morphology of the samples in Fig. 7 also shows that HAp sample exhibits a rod-like morphology, with a diameter of about 20 nm and a length of about 50 nm, whereas ClAp sample exhibits an irregular shape with a diameter of about 20 nm. It indicates the phase and particle morphology of the products are significantly affected by different calcium sources.

The specific surface areas and porous nature of the two samples were further investigated by means of nitrogen adsorption/desorption measurements, as shown in Fig. 8. According to the IUPAC classification, the isotherm is ascribed to a type IV with a type H_3 hysteresis loop, and the adsorption capacity increased quickly at a higher relative pressure range (P/P_0 > 0.9), indicating the existence of larger interparticle mesopores and macropores in the two samples. Therefore, the two samples both had a broad band ranging between 50 and 200 nm, which is ascribed to the texture porosity formed caused by nanoparticles aggregation. It can be noted that the porosity of the samples based on BJH method was consistent with that observed by SEM and TEM. Moreover, the BET surface area of the HAp and ClAp sample was 104.4 and 90.9 $m^2 \cdot g^{-1}$, respectively.

3.3. Application in water treatment

In this study, the adsorption performance of the two samples was investigated through the adsorptive removal of CR from simulated wastewater. The amount of adsorption was calculated by Eq. (1).

$$q_t = \frac{(C_0 - C_t)V}{W} \tag{1}$$

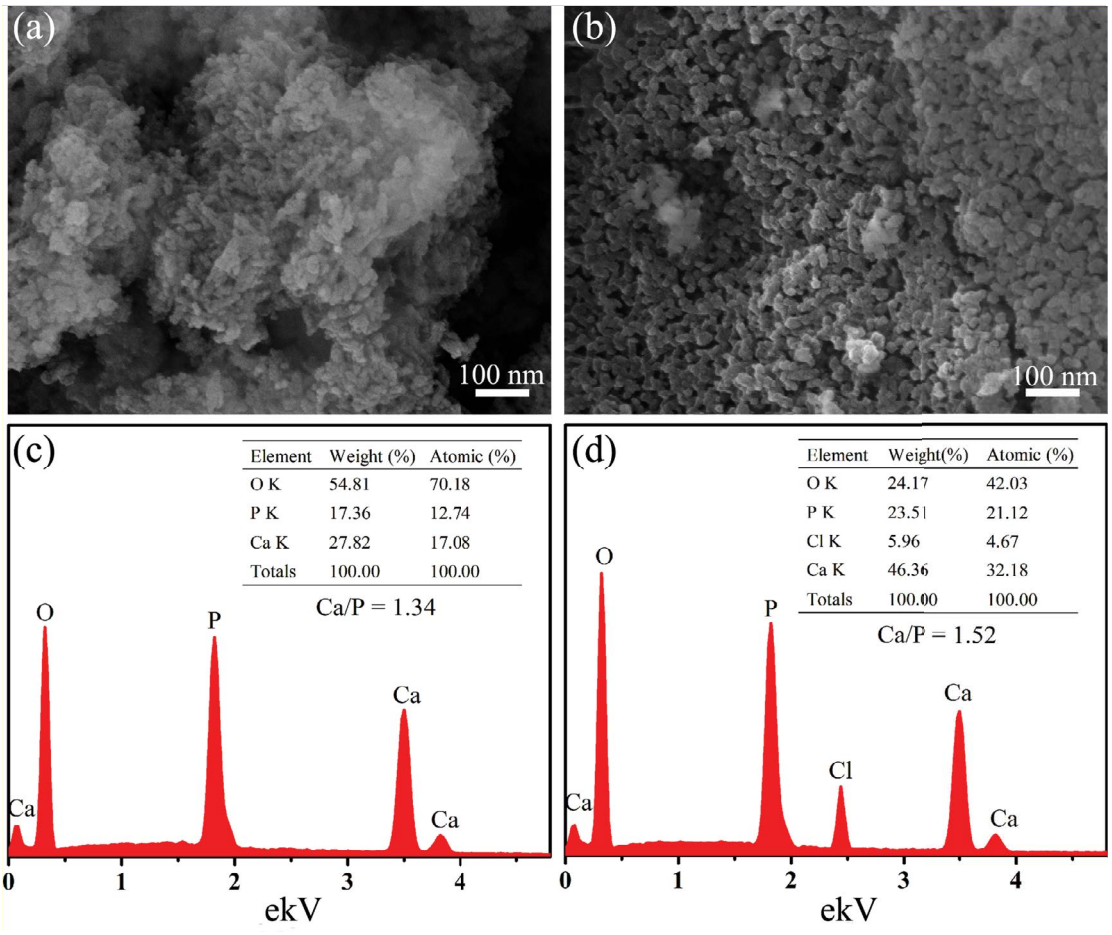

Fig. 6. SEM micrographs and energy-dispersive X-ray analysis for the powders (a) HAp and (b) ClAp.

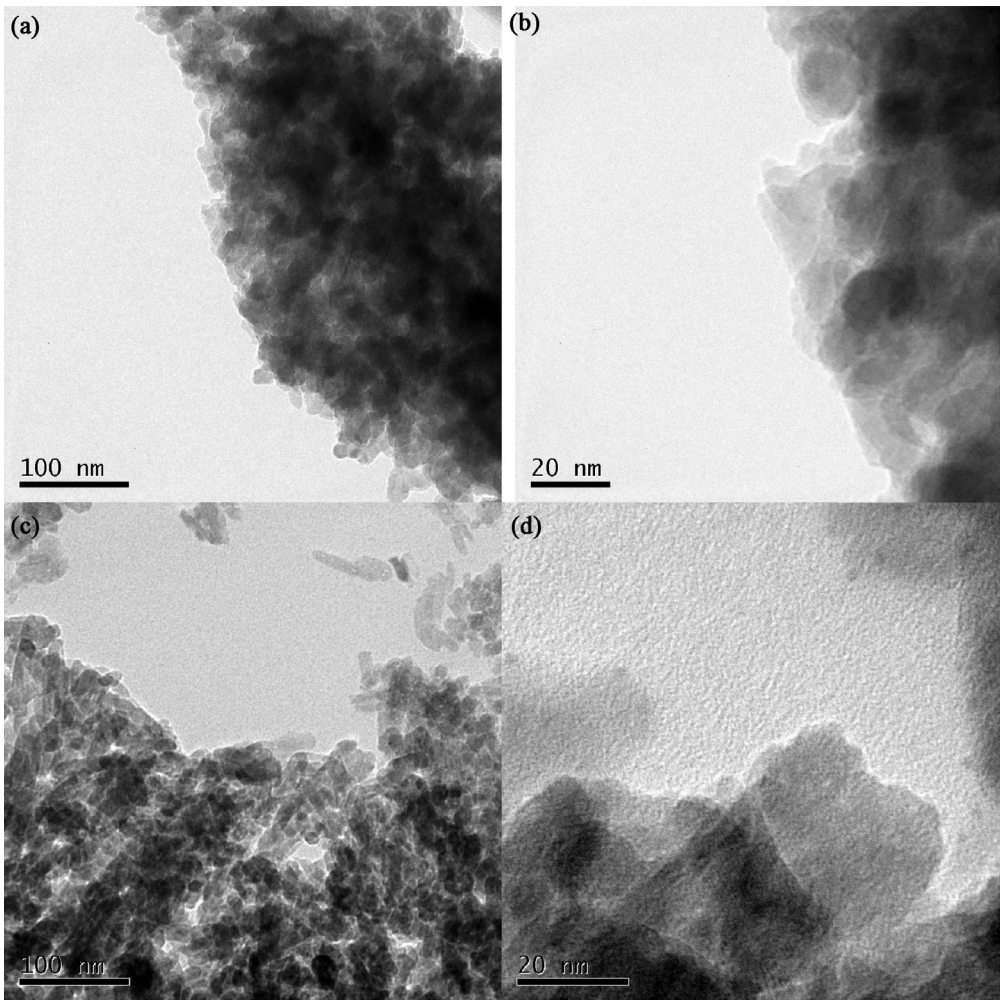

Fig. 7. TEM micrographs analysis for the powders (a,b) HAp, and (c,d) ClAp.

where C_0 is the initial concentration of CR (mg·L^{-1}), q_t (mg·g^{-1}) is the amount adsorbed per gram of absorbent at time t (min), C_t is the concentration of CR at time t of adsorption (mg·L^{-1}), V is the initial volume (L) the CR solution, and W is the weight of the absorbent (g).

The effect of the contact time was analyzed using the plot of q_t vs. t at different initial CR concentrations, as shown in Fig. 10a and b. Remarkably, the adsorption rates were extraordinarily high during the first 5 min at all concentrations for both of the two samples. The adsorption then proceeded slowly with contact time, and the equilibrium reached approximately after 120 min. The maximum CR adsorption capacity of HAp and ClAp was found to be 380.73 and 370.57 mg·g^{-1} at the initial concentrations of 500 mg·L^{-1}. Meanwhile, the removal efficiency was found to be 96.26%, 88.71% and 76.15% for HAp sample, and 92.34%, 83.10% and 74.11% for ClAp sample at the initial CR concentrations of 100, 300 and 500 mg·L^{-1}, respectively.

Fig. 9 shows the adsorption spectra of CR solution at a constant initial concentration of 100 mg·L^{-1} in the presence of the HAp sample for various durations in the adsorption process. The intensity of adsorption peak corresponding to the CR molecule at 498 nm decreases gradually as the adsorption times increases and almost completely disappears after about 180 min.

To understand the characteristics of the adsorption process, the kinetics of CR adsorption on the two samples was investigated by using pseudo-first-order and pseudo-second-order kinetic models, and the Eqs. (2) and (3):

$$\log\left(q_e - q_t\right) = \log q_e - \frac{k_1 t}{2.303} \tag{2}$$

$$\frac{t}{q_t} = \frac{1}{k_2 q_e^2} + \frac{t}{q_e} \tag{3}$$

where q_e and q_t (mg·g^{-1}) are the amounts of adsorption at equilibrium and at any time t (min), respectively. k_1 (min^{-1}) and k_2 (g·mg^{-1}·min^{-1}) are the pseudo-first-order and pseudo-second-order rate constants, respectively. The kinetic parameters and the correlation coefficients (R^2) are listed in Table 2. The pseudo-second-order model fits well with experimental date at all the initial concentrations with high correlation coefficients, and the values of $q_{e,\text{cal}}$ are very close to the experimentally observed values of $q_{e,\text{exp}}$. These results indicate that the adsorption system under study belongs to

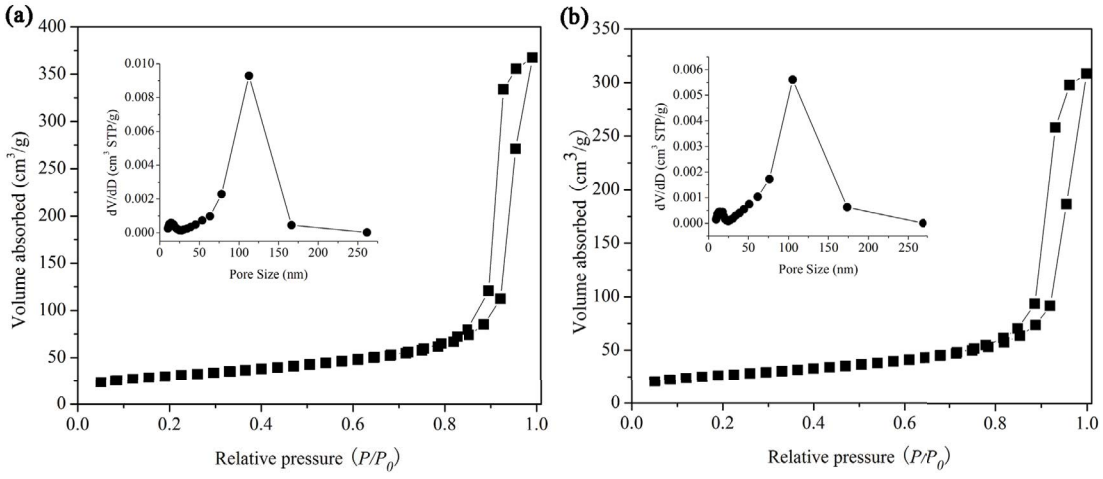

Fig. 8. Nitrogen adsorption–desorption isotherms and pore-size distribution (inset) of the powders (a) HAp and (b) ClAp.

Table 2
Kinetic parameters for the adsorption of CR onto HAp and ClAp samples

Sample	C_0 (mg·L^{-1})	$q_{e,exp}$ (mg·g^{-1})	Pseudo-first-order			Pseudo-second-order		
			k_1 (g·mg^{-1}·min^{-1})	$q_{e,cal}$ (mg·g^{-1})	R^2	k_2 (g·mg^{-1}·min^{-1})	$q_{e,cal}$ (mg·g^{-1})	R^2
HAp	100	96.26	0.3961	93.90	0.99577	0.01137	96.02	0.99783
	300	266.12	0.2050	243.29	0.95521	0.0012	260.01	0.98857
	500	380.73	0.1036	352.43	0.95071	0.00039	385.16	0.98827
ClAp	100	92.34	0.2975	86.10	0.98832	0.00655	89.58	0.99669
	300	249.30	0.1274	210.34	0.87586	0.00075	230.89	0.96465
	500	370.57	0.0471	325.89	0.89286	0.00018	364.51	0.95753

the pseudo-second-order kinetic model. The $q_{e,cal}$ increased with increasing the initial concentration, due to the relatively strong driving force of the concentration gradient at high concentrations. The value of pseudo-second-order rate constants decreased from 0.01137 to 0.00039 for HAp sample, and 0.00655 to 0.00018 for ClAp sample, which is ascribed to the lower competition for the surface-active sites at lower concentration.

Adsorption capacity at different aqueous equilibrium concentration can be illustrated by the adsorption isotherm. Two well-known models, Langmuir and Freundlich isotherm, were selected to analyze the equilibrium adsorption date. The isotherm models can be expressed as follows:

$$q_e = \frac{q_m K_L C_e}{1 + K_L C_e} \tag{4}$$

$$q_e = K_F C_e^{1/n} \tag{5}$$

where C_e is equilibrium (residual) concentration of solute (mg·L^{-1}), q_e is the amount of adsorbed at equilibrium (mg·g^{-1}), q_m is the maximum adsorption capacity and K_L is the Langmuir adsorption model constant (L·mg^{-1}). In the Freundlich equation, K_F is the adsorption model constant (L·g^{-1}) and n is Freundlich adsorption model exponent. The related parameters obtained from the two isotherm models are listed in Table 3. Fig. 10c and d show that the adsorption of CR onto the HAp and ClAp can both be better described by the Langmuir model, with a correlation coefficient R^2 value of 0.97657 and 0.96381, respectively,

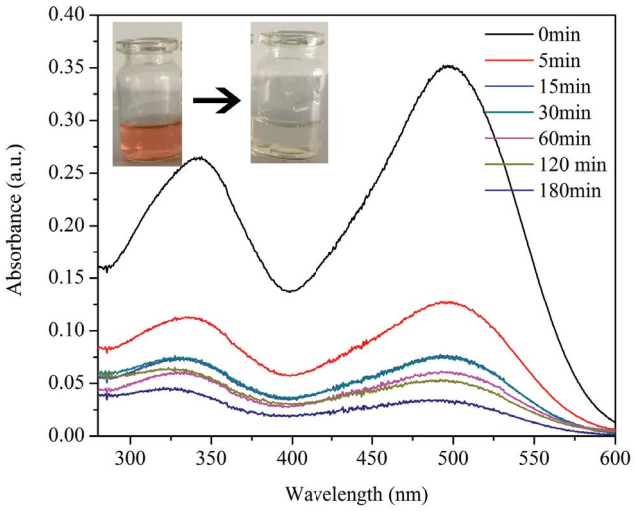

Fig. 9. UV-Vis adsorption spectra change of CR (100 mg·L^{-1}) after being treated by HAp absorbent.

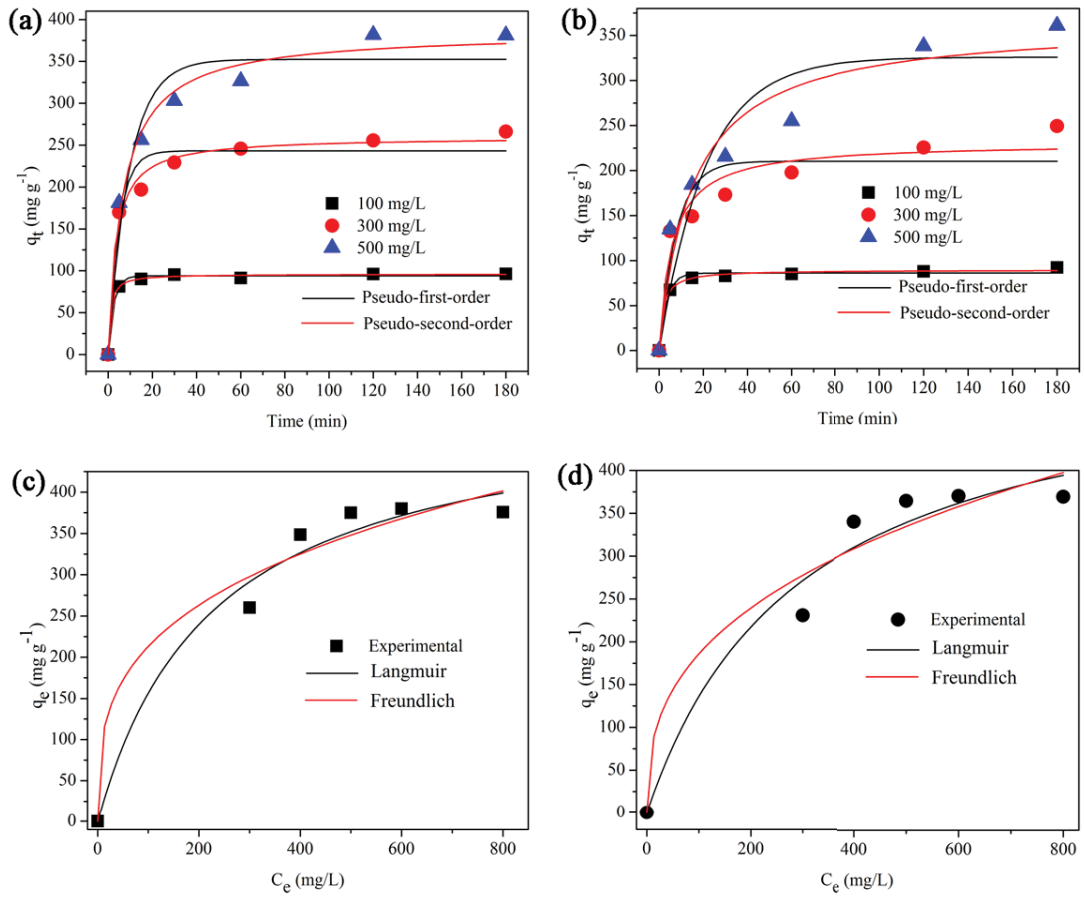

Fig. 10. Kinetics plots of CR adsorption on (a) HAp absorbent, and (b) ClAp absorbent, adsorption isotherm curves of CR adsorption on the (c) HAp absorbent, and (d) ClAp absorbent.

Table 3
Isotherm parameters for the adsorption of CR onto HAp and ClAp samples

Sample	Langmuir			Freundlich		
	q_m (mg·g^{-1})	K_L (L·mg^{-1})	R^2	K_F	n	R^2
HAp	512.78	0.00439	0.97657	52.32	0.30488	0.96823
ClAp	542.27	0.00336	0.96381	34.52	0.36553	0.95328

Table 4
Comparison of the maximum CR dye adsorption capacities of various adsorbents determined by Langmuir isotherm model

Adsorbents	Adsorption capacities (mg·g^{-1})	S_{BET} (m^2·g^{-1})	References
HAp	512.78	104.4	This study
ClAp	542.27	90.90	This study
HAp	337.33	82.94	[29]
HAp	495.56	–	[30]
HAp	139	135	[31]
Fe_3O_4@ClAp	370.4	90.43	[32]
Fe_3O_4/NiO nanocomposite	210.78	148.53	[33]
NiO microspheres	456.8	185.1	[34]
Fe_3O_4@bacteria	320.1	–	[35]

which indicates that the adsorption process is slightly superior to the Langmuir model. The maximum adsorption capacity (q_m) for the HAp and ClAp sample as calculated using the non-linear simulation equation was 512.78 and 542.27 mg·g^{-1}, respectively.

Table 4 compares the maximum adsorption capacity of HAp and ClAp with various absorbents previously used for removal of CR in water. The results showed that the HAp and ClAp absorbents used in this study possessed much higher adsorption capacity to CR than previously reported apatite absorbent [29–32]. In the meantime, this value is even higher than that of previously reported nano-structured absorbents, such as, Fe_3O_4/NiO nanocomposite (210.78 mg·g^{-1}) [33], NiO microspheres (456.8 mg·g^{-1}) [34], and Fe_3O_4@bacteria (320.1 mg·g^{-1}) [35]. These observations clearly emphasize that the HAp and ClAp presented in this study is a potential absorbent material for organic dyes contaminants.

4. Conclusion

In summary, HAp and ClAp nanostructure powders were prepared by a novel precipitation route with different calcium sources. The powders exhibited an extraordinary adsorption capacity and fast adsorption rates for CR in water due to their large specific surface areas and mesoporous structure. The maximum adsorption capacity of HAp and ClAp for CR was 512.78 and 542.27 mg·g^{-1}, respectively. Furthermore, the kinetics and isotherm of adsorption process were found to obey the pseudo-second-order kinetics and Langmuir isotherm models. The apatite HAp and ClAp are potential for application in the dye-polluted water purification.

References

[1] M.W. Shahzad, M. Burhan, L. Ang, K.C. Ng, Energy-water-environment nexus underpinning future desalination sustainability, Desalination, 413 (2017) 52–64.

[2] K.C. Ng, M. Burhan, Q. Chen, D. Ybyraiykul, F.H. Akhtar, M. Kumja, R.W. Field, M.W. Shahzad, A thermodynamic platform for evaluating the energy efficiency of combined power generation and desalination plants, npj Clean Water, 4 (2021) 25, doi: 10.1038/s41545-021-00114-5.

[3] M.W. Shahzad, M. Burhan, K.C. Ng, A standard primary energy approach for comparing desalination processes, npj Clean Water, 2 (2019) 1, doi: 10.1038/s41545-018-0028-4.

[4] S.H. Teo, C.H. Ng, A. Islam, G. Abdulkareem-Alsultan, C.G. Joseph, J. Janaun, Y.H. Taufiq-Yap, S. Khandaker, G.J. Islam, H. Znad, M.R. Awual, Sustainable toxic dyes removal with advanced materials for clean water production: a comprehensive review, J. Clean. Prod., 332 (2022) 130039, doi: 10.1016/j.jclepro.2021.130039.

[5] M. Shabir, M. Yasin, M. Hussain, I. Shafiq, P. Akhter, A.S. Nizami, B.H. Jeon, Y.K. Park, A review on recent advances in the treatment of dye-polluted wastewater, J. Ind. Eng. Chem., 112 (2022) 1–19.

[6] D. Vishnu, B. Dhandapani, S. Authilingam, S.V.A. Sivakumar, Comprehensive review of effective adsorbents used for the removal of dyes from wastewater, Curr. Anal. Chem., 18 (2022) 255–268.

[7] P. Nnaji, C. Anadebe, O.D. Onukwuli, Application of experimental design methodology to optimize dye removal by *Mucuna sloanei* induced coagulation of dye-based wastewater, Desal. Water Treat., 198 (2020) 396–406.

[8] A. Giwa, A. Yusuf, H.A. Balogun, N.S. Sambudi, M.R. Bilad, I. Adeyemi, S. Chakraborty, S. Curcio, Recent advances in advanced oxidation processes for removal of contaminants from water: a comprehensive review, Process Saf. Environ. Prot., 146 (2021) 220–256.

[9] P. Franco, S. Cardea, A. Tabernero, I. De Marco, Porous aerogels and adsorption of pollutants from water and air: a review, Molecules, 26 (2021) 4440, doi: 10.3390/molecules26154440.

[10] H. Jo, Y. Choi, T.H. Le, H. Lee, M. Kim, J. Lee, H. Yoon, Iron/carbon nanofibers as Fenton catalysts for the electrochemical detection and degradation of dye pollutants, ACS Appl. Nano Mater., 4 (2021) 11007–11016.

[11] D. Vishnu, B. Dhandapani, S. Authilingam, S.V.A. Sivakumar, Comprehensive review of effective adsorbents used for the removal of dyes from wastewater, Curr. Anal. Chem., 18 (2022) 255–268.

[12] J.F. Zhao, K. Yan, X.M. Wen, H.S. Xu, Solution combustion synthesis of porous MgO nanostructures for efficient removal of Congo red, J. Nanosci. Nanotechnol., 20 (2019) 810–818.

[13] Z.C. Wang, Z. Tang, X.D. Xie, M.Q. Xi, J.F. Zhao, Salt template synthesis of hierarchical porous carbon adsorbents for Congo red removal, Colloids Surf., A, 648 (2022) 129278, doi: 10.1016/j.colsurfa.2022.129278.

[14] F.S.A. Khan, N.M. Mubarak, Y.H. Tan, M. Khalid, R.R. Karri, R. Walvekar, E.C. Abdullah, S. Nizamuddin, S.A.A. Mazari, A comprehensive review on magnetic carbon nanotubes and carbon nanotube-based buckypaper for removal of heavy metals and dyes, J. Hazard. Mater., 413 (2021) 125375, doi: 10.1016/j.jhazmat.2021.125375.

[15] J.F. Zhao, J.C. Zha, H.B. Lu, C. Yang, K. Yan, X.K. Meng, Cauliflower-like Ni/NiO and NiO architectures transformed from nickel alkoxide and their excellent removal of Congo red and Cr(VI) ions from water, RSC Adv., 6 (2016) 103585–103593.

[16] Z.C. Wang, J.F. Zhao, S.L. Yin, Solution combustion synthesis of CeO_2 powders and its application in water treatment, Int. J. Appl. Ceram. Technol., 19 (2022) 2990–2997.

[17] J.F. Zhao, X.M. Wen, H.S. Xu, Y.C. Weng, Y.Q. Chen, Fabrication of recyclable magnetic biosorbent from eggshell membrane for efficient adsorption of dye, Environ. Technol., 42 (2021) 4380–4392.

[18] M. Supova, Substituted hydroxyapatites for biomedical applications: a review, Ceram. Int., 41 (2015) 9203–9231.

[19] M. Ibrahim, M. Labaki, J.M. Giraudon, J.F. Lamonier, Hydroxyapatite, a multifunctional material for air, water and soil pollution control: a review, J. Hazard. Mater., 383 (2020) 121139, doi: 10.1016/j.jhazmat.2019.121139.

[20] X.H. Xu, H.L. Wang, J.F. Wu, Z.C. Chen, X.Y. Zhang, M.Q. Li, Hydrothermal *in-situ* synthesis and anti-corrosion performance of zinc oxide hydroxyapatite nanocomposite anti-corrosive pigment, Coatings, 12 (2022) 420, doi: 10.3390/coatings12040420.

[21] C.R.D. Ferreira, A.A.G. Santiago, R.C. Vasconcelos, D.F.F. Paiva, F.Q. Pirih, A. Araujo, F.V. Motta, M.R.D. Bomio, Study of microstructural, mechanical, and biomedical properties of zirconia/hydroxyapatite ceramic composites, Ceram. Int., 48 (2022) 12376–12386.

[22] E.J.M. Edralin, J.L. Garcia, F.M. dela Rosa, E.R. Punzalan, Sonochemical synthesis, characterization and photocatalytic properties of hydroxyapatite nano-rods derived from mussel shells, Mater. Lett., 196 (2017) 33–36.

[23] M. Bin Mobarak, M.S. Hossain, Z. Yeasmin, M. Mahmud, M.M. Rahman, S. Sultana, S.M. Masum, S. Ahmed, Probing the photocatalytic competency of hydroxyapatite synthesized by solid state and wet chemical precipitation method, J. Mol. Struct., 1252 (2022) 132142, doi: 10.1016/j.molstruc.2021.132142.

[24] A. Huang, H.L. Dai, X.P. Wu, Z. Zhao, Y.Z. Wu, Synthesis and characterization of mesoporous hydroxyapatite powder by microemulsion technique, J. Mater. Res. Technol., 8 (2019) 3158–3166.

[25] I. Fatimah, G.R. Aulia, W. Puspitasari, R. Nurillahi, L. Sopia, R. Herianto, Microwave-synthesized hydroxyapatite from paddy field snail (*Pila ampullacea*) shell for adsorption of bichromate ion, Sustainable Environ. Res., 28 (2018) 462–471.

[26] A. Ito, Y. Otsuka, M. Takeuchi, H. Tanaka, Mechanochemical synthesis of chloroapatite and its characterization by powder

X-ray diffractometory and attenuated total reflection-infrared spectroscopy, Prog. Colloid Polym. Sci., 295 (2017) 2011–2018.
[27] J.F. Zhao, J.J. Zhao, J.H. Chen, X.H. Wang, Z.D. Han, Y.H. Li, Rietveld refinement of hydroxyapatite, tricalcium phosphate and biphasic materials prepared by solution combustion method, Ceram. Int., 40 (2014) 3379–3388.
[28] R.A. Bohara, N.D. Thorat, H.M. Yadav, S.H. Pawar, One-step synthesis of uniform and biocompatible amine functionalized cobalt ferrite nanoparticles: a potential carrier for biomedical application, New J. Chem., 38 (2014) 2979–2986.
[29] Y.B. Guan, W.C. Cao, X.H. Wang, A. Marchetti, Y.Z. Tu, Hydroxyapatite nano-rods for the fast removal of Congo red dye from aqueous solution, Mater. Res. Express, 5 (2018) 065053, doi: 10.1088/2053-1591/aaccb8.
[30] H.B. Wang, K.Q. Yan, J.D. Chen, Preparation of hydroxyapatite microspheres by hydrothermal self-assembly of marine shell for effective adsorption of Congo red, Mater. Lett., 304 (2021) 130573, doi: 10.1016/j.matlet.2021.130573.
[31] H. Bensalah, S.A. Younssi, M. Ouammou, A. Gurlo, M.F. Bekheet, Azo dye adsorption on an industrial waste-transformed hydroxyapatite adsorbent: kinetics, isotherms, mechanism and regeneration studies, J. Environ. Chem. Eng., 8 (2020) 103807, doi: 10.1016/j.jece.2020.103807.
[32] J. Wang, Y.L. Liu, H.Y. Xie, P.Y. Li, X. Chen, W.R. Hu, Y.B. Wang, Y.K. Zhang, Facile synthesis of a magnetic chlorapatite composite with a high efficiency and recyclable adsorption for Congo red, Mater. Res. Express, 6 (2019) 116118, doi: 10.1088/2053-1591/ab4b9c.
[33] P. Koohi, A. Rahbar-kelishami, H. Shayesteh, Efficient removal of Congo red dye using Fe_3O_4/NiO nanocomposite: synthesis and characterization, Environ. Technol. Innovation, 23 (2021) 101559, doi: 10.1016/j.eti.2021.101559.
[34] Y. Jia, J. Ni, P.Y. Wu, F. Fang, Y.X. Zhang, Fast removal of Congo red from aqueous solution by adsorption onto micro/nanostructured NiO microspheres, Mater. Sci. Eng., B, 270 (2021) 115228, doi: 10.1016/j.mseb.2021.115228.
[35] Y.R. Pi, C.Y. Duan, Y.L. Zhou, S.J. Sun, Z.D. Yin, H.C. Zhang, C.F. Liu, Y. Zhao, The effective removal of Congo red using a bio-nanocluster: Fe_3O_4 nanoclusters modified bacteria, J. Hazard. Mater., 424 (2022) 127577, doi: 10.1016/j.jhazmat.2021.127577.